

---

# EMERGENT SELF-SIMILARITY AND SCALING PROPERTIES OF FRACTAL INTRA-URBAN HEAT ISLETS FOR DIVERSE GLOBAL CITIES

---

A PREPRINT

IN REVIEW WITH PHYSICAL REVIEWS E

**Anamika Shreevastava<sup>1,\*</sup>, P. Suresh C. Rao<sup>1</sup>, Gavan S. McGrath<sup>2,3</sup>**

1. Lyles School of Civil Engineering, Purdue University, West Lafayette, IN, USA

2. School of Earth and Environment, The University of Western Australia, Perth, Australia

3. Ecosystem Science, Department of Biodiversity Conservation and Attractions, Kensington, WA, Australia

\*Corresponding author: ashreeva@purdue.edu; <http://anamika255.github.io>

August 31, 2019

## ABSTRACT

1 Urban areas experience elevated temperatures due to the Urban Heat Island (UHI) effect. However,  
2 temperatures within cities vary considerably and their spatial heterogeneity is not well character-  
3 ized. Here, we use Land Surface Temperature (LST) of 78 global cities to show that the Surface  
4 UHI (SUHI) is fractal. We use percentile-based thermal thresholds to identify heat clusters emerg-  
5 ing within SUHI and refer to them collectively as intra-urban heat *islets*. The islets display prop-  
6 erties analogous to that of a percolating system as we vary the thermal thresholds. At percolation  
7 threshold, the size distribution of these islets in all cities follows a power-law, with a scaling ex-  
8 ponent ( $\beta$ ) of 1.88 ( $\pm 0.23$ , 95%CI) and an aggregated Perimeter Fractal Dimension ( $D$ ) of 1.33  
9 ( $\pm 0.064$ , 95%CI). This commonality indicates that despite the diversity in urban form and function  
10 across the world, the urban temperature patterns are different realizations with the same aggregated  
11 statistical properties. Furthermore, we observe the convergence of these scaling exponents as the  
12 city sizes increase. Therefore, while the effect of diverse urban morphologies is evident in smaller  
13 cities, in the mean, the larger cities are alike. Lastly, we calculate the mean islet intensities, i.e.  
14 the difference between mean islet temperature and thermal threshold, and show that it follows an  
15 exponential distribution, with rate parameter,  $\lambda$ , for all cities.  $\lambda$  varied widely across the cities and  
16 can be used to quantify the spatial heterogeneity within SUHIs. In conclusion, we present a basis for  
17 a unified characterization of urban heat from the spatial scales of an urban block to a megalopolis.

## 18 **1 Introduction**

19 Cities are the apex examples of complex, coupled, socio-technological systems, which are projected to account for  
20 more than 70% of the global population by 2050 (Seto and Shepherd, 2009). Rapid urbanization presents multiple  
21 challenges, among them the Urban Heat Island (UHI) effects. Urban heat stress is predicted to be more frequent  
22 and persistent in the coming century due to a synergistic effect of mesoscale heat waves and the UHI (Li and Bou-  
23 Zeid, 2013; Meehl and Tebaldi, 2004; Allen et al., 2014). Metrics such as UHI Intensity, that quantify the difference  
24 between a representative (often the mean) urban and neighboring non-urban air temperature, fail to characterize *intra*-  
25 urban spatial variability (Debbage and Shepherd, 2015; Stewart and Oke, 2012). Furthermore, critical hot regions can  
26 emerge within the heat island itself. Therefore, for optimizing mitigation efforts and targeting scarce resources where  
27 they are most warranted, it is critical to characterize the spatial heterogeneity that arises within a city (Rosenzweig  
28 et al., 2010).

29 Cities tend to be warmer because of an increase in heat sources, such as excessive built-up area, industries, and air-  
30 conditioning exhausts, and a scarcity of heat sinks (e.g., vegetation and water bodies) (Oke, 1982). Spatial organization  
31 of physical assets, i.e., the urban form (e.g., impervious areas; buildings), as well as mobile assets such as automobile  
32 govern the distribution of heat sources in a city and modify the cooling effect of heat sinks. Prior research has shown  
33 that urban form has numerous fractal properties related to land use (Batty and Longley, 1994), urban infrastructure  
34 networks (Yang et al., 2017; Krueger et al., 2017), and impervious area (Chen, 2010; Makse et al., 1998). Similarly,  
35 the metabolic functions of cities (Oke, 1982) display scaling in the spatial patterns of population distribution, traffic,  
36 and energy use among others (Gonzalez et al., 2008; Rozenfeld et al., 2008; Bettencourt and West, 2010). While  
37 similar scaling laws and fractal metrics have also been developed in atmospheric sciences (Lovejoy and Schertzer,  
38 1986), their application in UHI studies remains limited (Weng, 2003; Debbage and Shepherd, 2015). Comprehensive  
39 scaling laws that describe spatio-temporal variability of intra-urban high heat clusters have not been explored yet.

40 Based on the established correlation of surface temperatures and urban morphology (Buyantuyev and Wu, 2010;  
41 Zhou et al., 2011; Liu and Weng, 2009), we hypothesize that SUHI patterns should exhibit a fractal spatial structure.  
42 We analyze Landsat 8 derived LST data for 78 diverse cities across the world and use percentile-based thermal thresh-  
43 olds and clustering techniques from percolation theory to identify clusters of high heat within cities. Here, we refer  
44 to the collection of heat clusters as intra-urban heat islets, which combine to form the UHI as a whole. First, we  
45 demonstrate the statistical self-similarity of heat islets. We then identify the scaling laws that quantify their size and  
46 intensity distributions, thereby, developing new metrics for spatial characterization of SUHIs.

## 47 **2 Methodology**

### 48 **2.1 Data**

49 We initially sampled a wide variety of global cities, including but not limited to the C-40 (<http://www.c40.org/cities>),  
50 that are representative of diverse climate types (Peel et al., 2007) as well as cultural backgrounds. Since the focus of  
51 this study is intra-urban heat islets, only the cities that exhibited elevated temperatures within the urban boundaries  
52 were selected. Cities which showed inversion of the heat island effect (Lazzarini et al., 2013) or contained significant  
53 topographic relief dominating the LST patterns were removed from the sample. The resulting sample set consists of 78  
54 cities with populations ranging from 200k to 30M. It includes densely packed urban areas, such as Seoul and Beijing,  
55 agglomerated cities such as Mexico City, highly heterogeneous cities like Mumbai, and highly structured, grid-like  
56 cities such as Los Angeles and Houston. It should be noted that the selected list is not exhaustive in any way but a  
57 representative subset of diverse global cities. Complete list of cities studied and their Landsat image used is attached  
58 as Dataset S1 of Supplementary Material.

59 For obtaining spatially rich datasets for intra-urban studies, satellite-based observations have proven increasingly  
60 useful. Remotely sensed Land Surface Temperature (LST) is used as an indicator to characterize the Surface Urban  
61 Heat Island (SUHI) (Voogt and Oke, 2003). Furthermore, uniformity in data quality of remotely sensed observations  
62 enables multi-city comparisons (Imhoff et al., 2010; Peng et al., 2011; Zhou et al., 2013). The geospatial analysis was  
63 implemented using Google Earth Engine (GEE) (Gorelick et al., 2017) to filter out cloud-free summertime days with  
64 an incident solar angle of at least 60 degrees for the selected cities. Figure 2 serves to visualize the geospatial format of  
65 data collected using the example of Boston, USA, and Kolkata, India. Land Surface Temperature (LST) was derived  
66 by a Single Channel Algorithm as detailed in (Walawender et al., 2012) using data from Landsat 8 (Bands 4, 5, 10,  
67 and 11) daytime images at a resolution of 90m (Figs 2b, and 2f). See Appendix A for algorithm and Dataset S1 further  
68 information on Landsat scenes used. For each city, the urban area was estimated using Land Cover Type dataset of  
69 Moderate-resolution Imaging Spectroradiometer (MODIS) - MCD12Q1 (Figs 2a, and 2e). The exact definition of  
70 urban boundaries and city area plays a significant role in urban scaling laws where different urban extents can produce  
71 different scaling exponents (Cottineau et al., 2017), therefore, a buffer of 5 km in the rural regions was taken to account  
72 for the peri-urban settlements. However, as the heat islets occur well within the city boundaries, the scaling exponents  
73 were found to be independent of the buffer width. Lastly, in case of coastal cities, the Large Scale International  
74 Boundary (LSIB) dataset provided by United States Office of the Geographer was used to crop out the oceans and  
75 delineate coastal boundaries within the GEE environment.

## 76 2.2 Heat Islets clustering and fractal analysis

77 We conceptualize the thermal map as a Digital Elevation Model (DEM) where temperatures substitute for elevation  
78 (See figure 7 in Appendix B). For each city, we select regions with temperatures above specified percentile thresholds  
79 ( $T_{thr}$ ) and group the connected regions together using a Moore neighborhood to define clusters, thereby identifying  
80 islets of higher heat for each incremental threshold (Shreevastava et al., 2018). In figure 2, we use the example of  
81 Boston and Kolkata to demonstrate the collection of islets appear at two different thermal thresholds, one correspond-  
82 ing to the percolation threshold, and another corresponding to the 95<sup>th</sup> percentile. At higher temperature thresholds  
83 we can delineate areas within cities that experience extreme temperatures. The use of thermal percentiles enables  
84 comparison between cities which differ in their background climates as apparent in figures 2b and 2f where the range  
85 of temperatures vary significantly between the two cities. We utilize two metrics to characterize the spatial complexity  
86 of these islets, as described below.

87 As a primary test of fractal structure, the aggregated Area-Perimeter fractal dimension (Mandelbrot, 1975) of the  
88 collection of islets is estimated at each  $T_{thr}$  using the following equation:

$$\Sigma P = k \cdot \Sigma A^{\frac{D}{2}} \quad (1)$$

89 where  $D$  is the fractal dimension,  $k = 2 * \sqrt{\pi} = 3.545$ , that is determined for the limiting case of a circle, and  
90 the summation of perimeters ( $P$ ) and areas ( $A$ ) goes over the set of islets (Batty and Longley, 1994). Note that we  
91 are referring to the fractal dimension of the ensemble iso-thermal contour lines here. In the limiting case of a circle,  
92  $P \propto \sqrt{A}$  and  $D = 1$ . For more irregular and convoluted shapes, the perimeter becomes increasingly plane-filling  
93 or elongated, resulting in the limit in linear shapes where  $P = A$  and  $D = 2$  (Figure 4a and 4b). For statistically  
94 self-similar surfaces, not only is  $D$  a fractional value between 1 and 2, but it is also the same for all thresholds used for  
95 clustering (Isichenko and Kalda, 1991).

96 Second, we examine the size distribution of islets. As  $T_{thr}$  is decreased, the total number of clusters increase as  
97 more regions with  $T > T_{thr}$  are selected. However, at the percolation threshold, the number of clusters start declining  
98 as they coalesce to form a giant connected component. This is illustrated in figure 3 using the example of Boston,  
99 USA. For fractal landscapes, clusters are statistically self-similar at the percolation threshold over certain ranges of  
100 sizes, with the cluster areas following a probability distribution with a power-law tail (Isichenko and Kalda, 1991).

101 This was first presented as an empirical rule by physicist and geographer Korcak (Imre and Novotný, 2016), who  
 102 suggested a general scaling law, now referred to as the Korcak’s law or the number-area rule, describing the size-  
 103 distribution of various geographical objects, including lakes and islands (Mandelbrot, 1975; Cael and Seekell, 2016).  
 104 This is expressed as the relative number of islands with an area equal to  $a$  is given by the power-law:  $N(a) \propto a^{-\beta}$ .  
 105 As an exceedance probability distribution function, the size distribution can be written as the following

$$P(A \geq a) \propto a^{1-\beta}, \quad \forall a \geq a_{min} \quad (2)$$

106 Above the percolation threshold, deviations from the power-law result in some form of tempering. We used a  
 107 conservative approach to test for and fit the power-law distributions using a combination of maximum-likelihood fitting  
 108 methods with goodness-of-fit tests based on the Kolmogorov Smirnov (KS) statistic and likelihood ratios (Clauset  
 109 et al., 2009) (See Appendix C for detailed methodology).

### 110 3 Results and Discussions

#### 111 3.1 Fractal Dimension

112 The aggregated area-perimeter Fractal Dimension ( $D$ ) of the heat islets was calculated for multiple values of  $T_{thr}$   
 113 (50<sup>th</sup>, 60<sup>th</sup>, ..., 90<sup>th</sup> percentiles). For each city,  $D$  is consistent for all values of  $T_{thr}$  as shown by the same  
 114  $\log(\text{Area}):\log(\text{Perimeter})$  ratio (Figure 4a and 4b). This is a key finding, demonstrating the statistical self-similarity  
 115 within SUHIs, empirically establishing fractal geometry of urban thermal landscape. Furthermore, the calculated val-  
 116 ues of  $D$  across all cities were approximately normally distributed with a mean  $D = 1.33$  and standard deviation  
 117 (s.d.) of 0.033. (see Figures 4c and 4d, see Dataset S3 of Supplementary Material for a complete list). Makse et al.,  
 118 (1998)(Makse et al., 1998) reported  $1.2 < D < 1.4$  for clusters of urban impervious areas, with a mean value of 1.33  
 119 as well. Another study reported  $1.22 \pm 0.08$  for 68 Chinese cities (Chen, 2010). Therefore, the fractal dimensions of  
 120 SUHI are in agreement with that of urban impervious area.

121  $D$  scaled weakly with city size as  $D = 0.0695 \cdot \log A_{city} + 1.15$  ( $R^2 = 0.7$ ) (Figure 4d). The tendency for  $D$  to  
 122 be smaller for small cities is reflective the varying urban morphology of cities as they grow. Smaller cities are often  
 123 mono-centric (more circle-like) with fewer heat islets, as a result, we would expect  $D$  to tend toward a value of 1.  
 124 While megalopolises, on the other hand, formed from agglomeration of multiple peri-urban settlements are expected  
 125 to have higher number of heat islets scattered throughout the city, thereby, increasing  $D$  (Figure 4d). This is also  
 126 reflected in the total number of islets for each city that scales linearly as  $N = 0.038 * A_{city} + 40$  ( $R^2 = 0.8$ ) (See  
 127 figure 8 in Appendix B). However, for self-affine surfaces, the total perimeter is dominated by the smallest islets, and  
 128 the total area is dominated by the largest island (Isichenko and Kalda, 1991). To examine the average shape of an  
 129 islet within a city, area-weighted mean fractal dimension (AWMFD) of the islets is a useful alternative (Debbage and  
 130 Shepherd, 2015). It is calculated using the following equation:

$$AWMFD = \sum_{i=1}^n \left[ \left( \frac{2 \ln \left( \frac{p_i}{k} \right)}{\ln a_i} \right) \left( \frac{a_i}{\sum_{i=1}^n a_i} \right) \right] \quad (3)$$

131 The AWMFD for cities were found to be approximately normally distributed as well with a mean AWMFD = 1.227  
 132 (s.d. = 0.025; See figure 9 in Appendix B).

### 133 3.2 Islet Size distribution

134 At the percolation threshold, the area-exceedance probability distribution was found to scale consistently with a power-  
 135 law tail for all cities, with the scaling exponent normally distributed with mean  $\beta = 1.88$  and s.d. = 0.12 (Figures 5a  
 136 and 5b). Alternative distributions, such as log-normal, exponential and Weibull, were tested as potential candidates;  
 137 however, they were all rejected (at  $p > 0.1$ ), while the same tests suggested that the distributions could not be rejected  
 138 as having power-law tails (See Appendix C and Dataset S2 of Supplementary Material).

139 The power-law size distribution is another key finding that further supports the observed fractal structure of heat  
 140 islets. The percolation threshold was found to be closely associated with the statistical mode of temperature distri-  
 141 bution, i.e. the most frequently encountered temperature in the city ( $R^2 = 0.93$ , see figure 10 in Appendix B). For  
 142 the case uncorrelated percolation,  $\beta$  is estimated to be 187/91 ( $\sim 2.05$ ) (Isichenko, 1992; Sahimi and Sahimi, 2014).  
 143 Moreover, empirical distributions of land classified as urban and cities modeled with correlated percolation as well  
 144 have found similar size distributions with  $\beta \sim 2$  (Makse et al., 1998; Fluschnik et al., 2016; Gangopadhyay and Basu,  
 145 2009). A slightly smaller exponent of 1.88, in this case, indicates a greater probability of occurrence of heat islets  
 146 than what would be expected from impervious area alone. Here, the power-law tails are curtailed on the higher end  
 147 by limits of the study domain i.e. the total city size, in this case, (Newman, 2005), and on the lower end, by spatial  
 148 resolution. Numerous smaller heat clusters are either not captured or are rounded off to integer multiples of the lowest  
 149 available resolution. Interestingly, in this case, the lower bound ( $a_{min}$  at which the power-law tail starts) is  $\sim 0.25$   
 150  $\text{km}^2$ , which corresponds to the size of a couple of urban blocks. This suggests that below this, the heat islets may  
 151 indeed scale differently as the individual building level features become evident. There is potential to extend this  
 152 analysis beyond these spatial scales, however, this was not the objective of this study. A relationship between  $D$  and  $\beta$   
 153 can be derived for Gaussian surfaces as  $\beta - 1 = D/2$  (Isichenko and Kalda, 1991). However, this was not found to be  
 154 true for heat islets indicating a departure from random Gaussian topography. Lastly, fractal landscapes are expected to  
 155 yield the same scaling exponents irrespective of the resolution. To test their sensitivity to input resolution, LST maps  
 156 were aggregated at a range of resolutions from 90 m to 720 m. Scaling exponents were found to be the same, adding  
 157 further support to the self-similar topography of SUHI.

158 At temperatures above the percolation threshold, the size distribution shows a deviation from power-law in the form  
 159 of exponential tempering (Clauset et al., 2009) suggesting a model more consistent with:

$$P(A \geq a) \propto a^{1-\beta} \cdot e^{-c(T_{thr}) \cdot a}, \quad \forall a \geq a_{min} \quad (4)$$

160 where  $c$  is a tempering coefficient that depends on the thermal threshold. As the  $T_{thr}$  moves further away from the  
 161 percolation threshold, more tempering is observed. In figure 5d, we show the average value of  $c$  obtained for each  
 162 city at thresholds above the percolation threshold, which we will refer to as  $\bar{c}$ . Note that the  $\bar{c}$  is observed to be larger  
 163 and more variable for small cities ( $A < 1,000 \text{ km}^2$ ), decreasing steadily for larger cities (Figure 5d). As a result,  
 164 larger cities show consistent power-law area distributions even at higher thermal thresholds. Exponential tempering  
 165 suggests a reduced probability of occurrence of large hot islets for smaller cities and conversely a higher likelihood of  
 166 encountering them as cities grow even for higher thresholds. Other factors such as urban geometry and disaggregation  
 167 of heat islets could influence  $\bar{c}$  as well but further research will be needed to test that.

### 168 3.3 Islet intensity distribution

169 For UHIs, the UHI Intensity is defined as the difference between the mean urban temperature and the mean background  
 170 temperature of surrounding non-rural regions. An analogous metric for the intra-urban heat islets is defined here as the  
 171 islet intensity,  $\Delta T$ , as the difference between the mean temperature of each islet and  $T_{thr}$ . This captures the question:  
 172 How much hotter are the islets than the threshold used to define them? The mean and standard deviation of  $\Delta T$  over

173 each islet within a city were found to be equal which, along with the shape of its distribution, were indicative that  $\Delta T$   
 174 for each city is exponentially distributed, i.e:

$$p(\Delta T) \propto e^{-\lambda \Delta T} \quad (5)$$

175 As a result, we model the islet intensity distribution with a single parameter,  $\lambda$  (Figure 6c and S6). Calculated at  
 176 the percolation threshold, the values of  $\lambda$  across cities display a log-normal distribution with a mean =  $2.25 \text{ K}^{-1}$  and  
 177 s.d. =  $1.47 \text{ K}^{-1}$  (Figure 6d; see Dataset S3 for a complete list). Furthermore, it shows convergence to the mean with  
 178 increasing city size as well (Figure 6e). At a thermal threshold corresponding to the rural background temperature,  
 179 this corresponds to the conventional metric of mean Urban Heat Island Intensity (Oke, 1982). The scaling observed  
 180 in the islet size and intensity distributions are analogous to the scaling laws known for areas and mean stages of lakes  
 181 and wetlands (Bertassello et al., 2018; Cael and Seekell, 2016) and can be used to build the empirical basis for an  
 182 investigation into the scaling theory of intra-urban heat islets.

### 183 3.4 Convergence in exponents as cities grow

184 The area scaling exponent,  $\beta$ , varies between 1.6 and 2.2 for small cities ( $a_{city} < 1000 \text{ km}^2$ ), but for the larger cities  
 185 it converges to the mean (see Figure 5c). One explanation for this is statistical, wherein for small cities there are not  
 186 enough islets obtained at 90 m resolution which results higher statistical fluctuations about the mean are observed  
 187 (Figure 8 in Appendix B). As the number of islets increases with city size, steady averaging is achieved that results in  
 188 convergence towards the mean. However, from an urban growth perspective, this behavior is consistent with several  
 189 other complex systems that operate within cities (Klinkhamer et al., 2017; Barthelemy, 2016). For smaller cities,  
 190 the variability reveals the influence of factors unrelated to city size (Cottineau et al., 2017). Land-use and urban  
 191 infrastructures grow through parallel processes of expansion and densification (Mohajeri et al., 2015). Dense city  
 192 centers beget more in-fill construction as it becomes a prime spot for economic development. At the same time,  
 193 sprawling suburbs keep pushing the city boundaries due to the high costs of the inner city. As a result, despite the  
 194 diversity that smaller cities possess, as the cities grow, they self-organize along a common trajectory (Batty, 2013).  
 195 Similar convergence is also observed in the islet intensity distribution,  $\lambda$  (Figure 6e). On the other hand, the exponential  
 196 tempering coefficient,  $\bar{c}$ , converges to 0 (Figure 5d), which means the mega-agglomerations approach a consistent  
 197 power law even at higher thresholds. This suggests an increase in the proportion of city area that is exposed to higher  
 198 temperatures (Zhou et al., 2017). This is also in agreement with the observed scaling of aggregated UHI Intensity with  
 199 the log of city size (Oke, 1973).

### 200 3.5 Application for assessments

201 The narrow distributions of scaling parameters and their convergence are also relevant to the field of urban climate  
 202 research, for instance, to model the heat exchange between hot areas and their colder surroundings (Oke, 1982).  
 203 Current numerical weather prediction models, such as Weather Research Forecast (WRF) (Chen et al., 2011), use  
 204 gridded data formats and, as a result, the perimeter of any heat islet is resolved to the minimum resolution (about  
 205  $\sim 1 - 9 \text{ km}^2$ ). This results in an under-estimation of urban perimeter boundary which is important for modeling heat  
 206 exchange across the urban-rural transect. A fractal perimeter of iso-thermal contour lines indicates a larger perimeter  
 207 of contact with cooler regions, which in turn enables a larger heat flux to dissipate from the heat islets. The inclusion  
 208 of a correction factor to simulate a rough and convoluted perimeter (with  $D \sim 1.33$ ) may improve the modeling of  
 209 such processes. Furthermore, as the scaling metrics are rather narrowly distributed across diverse cities, we expect  
 210 such a correction factor to be extendable across all urban areas.

211 For extreme heat exposure assessment of urban communities, however, analysis of SUHI alone is not enough. Heat-  
 212 stress assessment requires the joint consideration of air temperature and humidity (Oleson et al., 2015). Despite the

213 difference in absolute values of UHI and SUHI, similarities between spatial patterns of the surface and air temperatures  
 214 have been reported (Schwarz et al., 2012; Henry et al., 1989). Therefore, techniques of scaling based on SUHI patterns  
 215 can be extended to spatial clusters of UHI as well. The additional challenge is to better understand the superimposition  
 216 of intra-urban heat islets with the spatial distribution of vulnerable communities (Chapman et al., 2017), such as  
 217 the poor in mega-cities, the elderly, or critical urban infrastructure such as roads, power grids, and communication  
 218 networks (Seto et al., 2012; Creutzig et al., 2015).

## 219 **4 Summary**

220 We show that the spatial structure of Surface Urban Heat Island (SUHI) is strongly fractal for 78 diverse global  
 221 cities. As a result, it can be conceptualized as a collection of intra-urban heat islets that occur as local heat clusters  
 222 within the cities. The heat islets have remarkably similar spatial structure as characterized by the fractal dimension  
 223 ( $D$ ), as well as a power-law size distribution with exponent,  $\beta$  at the percolation threshold. This finding is rather  
 224 surprising given the diversity of geographic, and socioeconomic constraints in the population of cities studied. At  
 225 higher thermal thresholds, deviation from power law is observed in the form of an exponential tempering ( $c$ ), which  
 226 indicates reduced clustering of extreme heat. Further research into the relationship between urban morphology and  
 227 exponential tempering can provide some useful insights on urban design solutions for intra-urban heat mitigation.

228 The selection of a temperature threshold that defines extreme heat varies from region to region depending on their  
 229 climate. For instance, the National Oceanic and Atmospheric Administration (NOAA) issues a heat stress warning  
 230 above  $33^{\circ}\text{C}$  for some regions in the US, whereas in the tropical regions of India, up to  $40^{\circ}\text{C}$  does not warrant a  
 231 warning (<https://www.weather.gov/safety/heat-index>). In the absence of a standard definition, use of percentile thermal  
 232 threshold based on historical records have been recommended (Robinson, 2001). Similarly, instead of setting rural  
 233 temperature as a benchmark, we present a more flexible characterization of local thermal maxima in the form of islet  
 234 intensity,  $\Delta T$  (Equation 5), from a percentile-based threshold. Furthermore, as the pdf describing their distribution  
 235 follows an exponential distribution, the intensity parameter ( $\lambda$ ) can be used to characterize the heterogeneity of thermal  
 236 extremes and compare across cities. The proposed framework of identifying extreme heat clusters by using incremental  
 237 thresholds can be used to describe the patterns of extreme heat clusters in any thermal landscape.

238 While overarching metric such as the ones derived here do not help in answering specific questions pertaining to a  
 239 particular city, the convergence of the metrics with increasing size does suggest a common attractor for all cities. Both  
 240  $\lambda$  and  $c$  were observed to decrease as the cities grow in size indicating an increased likelihood of occurrence larger  
 241 and hotter heat islets for mega-cities indicating that their residents are at greater risk of extreme heat stress impacts.  
 242 This begs the question if this is an inevitable or a desirable trajectory for growing cities? Such questions are of critical  
 243 importance now, as billions of people add to the urban populations, especially in the developing countries of Africa and  
 244 Asia. Identifying the common statistical properties of the heat islets across diverse cities provides a means to escape  
 245 from the geographical malaise of the uniqueness of place, and provides a step towards the improved characterization  
 246 of the complex urban thermal landscape.

## 247 **Acknowledgments**

248 The authors thank the organizers and participants of a series of Complex Networks Synthesis workshops; co-hosted  
 249 by Purdue University, University of Florida, Helmholtz Centre for Environmental Research, UFZ, and Technical  
 250 University, Dresden, Germany; which creating a trans-disciplinary collaborative research environment and provided  
 251 critical input across multiple workshops. A.S. wants to thank the NASA Earth and Space Science Fellowship (Grant  
 252 number: 80NSSC17K0441) for funding. P.S.C.R. acknowledges the support from NSF Collaborative Research - RIPS  
 253 Type 2: Resilience Simulation for Water, Power and Road Networks (1441188) and the Lee A. Reith Endowment in  
 254 the Lyles School of Civil Engineering at Purdue University.

## 255 APPENDIX A: Estimation of Land Surface Temperature

256 The algorithm used to calculate the Land Surface Temperature is outlined below.

Step 1: TOA radiance

$$L_{\lambda} = M_L \cdot Q_{cal} + A_L \quad (6)$$

257 where,

258  $L_{\lambda}$  = TOA spectral radiance ( $W/m^2 * srad * \mu m$ )

259  $M_L$  = Band-specific multiplicative rescaling factor from the metadata (RADIANCE\_MULT\_BAND\_x, where x is the  
260 band number)

261  $A_L$  = Band-specific additive rescaling factor from the metadata (RADIANCE\_ADD\_BAND\_x)

262  $Q_{cal}$  = Quantized and calibrated standard product pixel values (DN)

Step 2: TOA Brightness Temperature

$$T = \frac{K_2}{\ln\left(\frac{K_1}{L_{\lambda}} + 1\right)} \quad (7)$$

263 where,

264  $T$  = At-satellite brightness temperature (K)

265  $L_{\lambda}$  = TOA spectral radiance ( $W/m^2 * srad * \mu m$ )

266  $K_1$  = Band-specific thermal conversion constant from the metadata (K1\_CONSTANT\_BAND\_x)

267  $K_2$  = Band-specific thermal conversion constant from the metadata (K2\_CONSTANT\_BAND\_x)

268 The band-specific values were obtained from the metadata file. These equations are used for both band 10 and  
269 11, to obtain the temperatures. However, to obtain the actual ground surface temperature, the emissivity needs to be  
270 calculated. The codes implemented in R here were derived and modified from ArcGIS toolbox(Walawender et al.,  
271 2012).

Step 3: Proportion of vegetation ( $P_v$ ) and Emmissivity ( $e$ ) is estimated from NDVI to estimate actual LST:

$$P_v = \frac{NDVI - NDVI_{min}}{(NDVI_{max} - NDVI_{min})^2} \quad (8)$$

$$e = 0.004 * P_v + 0.986 \quad (9)$$

$$LST = \frac{T}{1 + w * \frac{T}{\rho} * \ln(e)} \quad (10)$$

272 where,

273  $T$  = At satellite brightness temperature (K) as per equation 9

274  $w$  = Wavelength of emitted radiation ( $11.5 \mu m$ )

275  $\rho = h * \frac{c}{\sigma} = 14380 \mu m K$

276 ( $\sigma$  = Boltzmann constant =  $1.38 \times 10^{23} \frac{J}{K}$ )

277  $h$  = Plancks constant =  $6.626 \times 10^{34} Js$

278  $c$  = velocity of light =  $2.998 \times 10^8 \frac{m}{s}$ )

279  $e$  = emissivity as per equation 9

## 280 Appendix B: Additional Figures

281 Figures 7 to 10 are the additional figures attached at the end of this document.



## 282 APPENDIX C: Fitting Probability distribution functions

283 For fitting probability distributions to the cluster size distribution, a combination of maximum-likelihood fitting  
 284 methods with goodness-of-fit tests based on the Kolmogorov-Smirnov (KS) statistic and likelihood ratios were used  
 285 (Clauset et al., 2009). A step-by-step methodology as summarized in Box 1 of (Clauset et al., 2009) and outlined  
 286 below was followed with the help of R-code provided by Laurent Dubroca and Cosma Shalizi on Clauset’s website:  
 287 <http://tuvalu.santafe.edu/~aaronc/powerlaws/>.

- 288 1. Estimate the parameters  $x_{min}$  and  $\beta$  of the power-law model.
- 289 2. Calculate the goodness-of-fit between the data and the power law. If the resulting p-value is greater than 0.1,  
 290 the power law is a plausible hypothesis for the data, otherwise, it is rejected.
- 291 3. Compare the power law with alternative hypotheses via a likelihood ratio test. For each alternative, if the  
 292 calculated likelihood ratio is significantly different from zero, then its sign indicates whether or not the alter-  
 293 native is favored over the power-law model.

294 The data were tested for a power-law tail fit and compared against 4 other competing distributions - Exponential,  
 295 Lognormal, Stretched Exponential (Weibull), and Power-law with an exponential rate of tempering. The basic idea  
 296 behind the likelihood ratio test is to compute the likelihood of the data under two competing distributions. The one  
 297 with the higher likelihood is then the better fit. Alternatively, one can calculate the ratio of the two likelihoods, or  
 298 equivalently the logarithm R of the ratio, which is positive or negative depending on which distribution is better or  
 299 zero in the event of a tie. Furthermore, the p-value for the Log-likelihood Ratio is checked and an outcome is selected  
 300 only if the p-value is less than 0.1 (For a 90% confidence).

301 The cluster size distributions for all cities were tested at the percolation temperature, and all of the distributions  
 302 were found to qualify as a power-law tail (with a p-value of 0.1, i.e. 90% confidence). The lower cut-off for power  
 303 law was found to be under 500 m for most cities (95% CI one-sided), this roughly corresponds to the size of an urban  
 304 block implying that the scaling doesn’t extend to the length scales smaller than an urban block. On comparing against  
 305 the other distribution, we find that 9 of the 78 cities (11.54%) can *also* be described as a power-law with exponential  
 306 tempering:  $P(A > a) \propto a^{-(\beta-1)}e^{-c \cdot a}$  with low exponential rates ( $c < 0.05$ ). However, none of them have  
 307 likelihoods suggesting a Weibull, exponential, or lognormal describe the data better. The table with each city’s results  
 308 is attached as separate excel sheet (Table S2: Tests of fitting exceedance probability distributions).

## 309 References

- 310 Allen, M. R., and Coauthors, 2014: Ipcc fifth assessment synthesis report-climate change 2014 synthesis report.
- 311 Barthelemy, M., 2016: *The structure and dynamics of cities*. Cambridge University Press.
- 312 Batty, M., 2013: *The new science of cities*. Mit Press.
- 313 Batty, M., and P. A. Longley, 1994: *Fractal cities: a geometry of form and function*. Academic press.
- 314 Bertassello, L. E., P. S. C. Rao, J. W. Jawitz, G. Botter, P. V. Le, P. Kumar, and A. F. Aubeneau, 2018: Wetlandscape  
 315 fractal topography. *Geophysical Research Letters*, **45** (14), 6983–6991.
- 316 Bettencourt, L., and G. West, 2010: A unified theory of urban living. *Nature*, **467** (7318), 912.
- 317 Buyantuyev, A., and J. Wu, 2010: Urban heat islands and landscape heterogeneity: linking spatiotemporal variations  
 318 in surface temperatures to land-cover and socioeconomic patterns. *Landscape Ecology*, **25** (1), 17–33.
- 319 Cael, B. B., and D. A. Seekell, 2016: The size-distribution of earths lakes. *Scientific Reports*, **6**, 29 633.
- 320 Chapman, S., J. E. Watson, A. Salazar, M. Thatcher, and C. A. McAlpine, 2017: The impact of urbanization and  
 321 climate change on urban temperatures: a systematic review. *Landscape Ecology*, **32** (10), 1921–1935.

- 322 Chen, F., and Coauthors, 2011: The integrated wrf/urban modelling system: development, evaluation, and applications  
323 to urban environmental problems. *International Journal of Climatology*, **31** (2), 273–288.
- 324 Chen, Y., 2010: Characterizing growth and form of fractal cities with allometric scaling exponents. *Discrete Dynamics  
325 in Nature and Society*, **2010**.
- 326 Clauset, A., C. R. Shalizi, and M. E. Newman, 2009: Power-law distributions in empirical data. *SIAM Review*, **51** (4),  
327 661–703.
- 328 Cottineau, C., E. Hatna, E. Arcaute, and M. Batty, 2017: Diverse cities or the systematic paradox of urban scaling  
329 laws. *Computers, environment and urban systems*, **63**, 80–94.
- 330 Creutzig, F., G. Baiocchi, R. Bierkandt, P.-P. Pichler, and K. C. Seto, 2015: Global typology of urban energy use  
331 and potentials for an urbanization mitigation wedge. *Proceedings of the National Academy of Sciences*, **112** (20),  
332 6283–6288.
- 333 Debbage, N., and J. M. Shepherd, 2015: The urban heat island effect and city contiguity. *Computers, Environment and  
334 Urban Systems*, **54**, 181–194.
- 335 Fluschnik, T., S. Kriewald, A. García Cantú Ros, B. Zhou, D. E. Reusser, J. P. Kropp, and D. Rybski, 2016: The  
336 size distribution, scaling properties and spatial organization of urban clusters: a global and regional percolation  
337 perspective. *ISPRS International Journal of Geo-Information*, **5** (7), 110.
- 338 Gangopadhyay, K., and B. Basu, 2009: City size distributions for india and china. *Physica A: Statistical Mechanics  
339 and its Applications*, **388** (13), 2682–2688.
- 340 Gonzalez, M. C., C. A. Hidalgo, and A.-L. Barabasi, 2008: Understanding individual human mobility patterns. *Nature*,  
341 **453** (7196), 779.
- 342 Gorelick, N., M. Hancher, M. Dixon, S. Ilyushchenko, D. Thau, and R. Moore, 2017: Google earth engine: Planetary-  
343 scale geospatial analysis for everyone. *Remote Sensing of Environment*, **202**, 18–27.
- 344 Henry, J. A., O. F. Wetterqvist, S. J. Roguski, and S. E. Dicks, 1989: Comparison of satellite, ground-based, and  
345 modeling techniques for analyzing the urban heat island. *Photogrammetric Engineering and Remote Sensing*, **55** (1),  
346 69–76.
- 347 Imhoff, M. L., P. Zhang, R. E. Wolfe, and L. Bounoua, 2010: Remote sensing of the urban heat island effect across  
348 biomes in the continental usa. *Remote Sensing of Environment*, **114** (3), 504–513.
- 349 Imre, A. R., and J. Novotný, 2016: Fractals and the korcak-law: a history and a correction. *The European Physical  
350 Journal H*, **41** (1), 69–91.
- 351 Isichenko, M., and J. Kalda, 1991: Statistical topography. i. fractal dimension of coastlines and number-area rule for  
352 islands. *Journal of Nonlinear Science*, **1** (3), 255–277.
- 353 Isichenko, M. B., 1992: Percolation, statistical topography, and transport in random media. *Reviews of Modern  
354 Physics*, **64** (4), 961.
- 355 Klinkhamer, C., E. Krueger, X. Zhan, F. Blumensaat, S. Ukkusuri, and P. S. C. Rao, 2017: Functionally fractal urban  
356 networks: Geospatial co-location and homogeneity of infrastructure. *arXiv preprint arXiv:1712.03883*.
- 357 Krueger, E., C. Klinkhamer, C. Urich, X. Zhan, and P. S. C. Rao, 2017: Generic patterns in the evolution of urban  
358 water networks: Evidence from a large asian city. *Physical Review E*, **95** (3), 032312.
- 359 Lazzarini, M., P. R. Marpu, and H. Ghedira, 2013: Temperature-land cover interactions: The inversion of urban heat  
360 island phenomenon in desert city areas. *Remote Sensing of Environment*, **130**, 136–152.
- 361 Li, D., and E. Bou-Zeid, 2013: Synergistic interactions between urban heat islands and heat waves: the impact in cities  
362 is larger than the sum of its parts. *Journal of Applied Meteorology and Climatology*, **52** (9), 2051–2064.
- 363 Liu, H., and Q. Weng, 2009: Scaling effect on the relationship between landscape pattern and land surface temperature.  
364 *Photogrammetric Engineering & Remote Sensing*, **75** (3), 291–304.

- 365 Lovejoy, S., and D. Schertzer, 1986: Scale invariance, symmetries, fractals, and stochastic simulations of atmospheric  
366 phenomena. *Bulletin of the American Meteorological Society*, **67** (1), 21–32.
- 367 Makse, H. A., J. S. Andrade, M. Batty, S. Havlin, H. E. Stanley, and Coauthors, 1998: Modeling urban growth patterns  
368 with correlated percolation. *Physical Review E*, **58** (6), 7054.
- 369 Mandelbrot, B. B., 1975: Stochastic models for the earth’s relief, the shape and the fractal dimension of the coastlines,  
370 and the number-area rule for islands. *Proceedings of the National Academy of Sciences*, **72** (10), 3825–3828.
- 371 Meehl, G. A., and C. Tebaldi, 2004: More intense, more frequent, and longer lasting heat waves in the 21st century.  
372 *Science*, **305** (5686), 994–997.
- 373 Mohajeri, N., A. Gudmundsson, and J.-L. Scartezzini, 2015: Expansion and densification of cities: Linking urban  
374 form to urban ecology. *International Conference on Future Buildings & Districts Sustainability from Nano to Urban*  
375 *Scale, Lausanne, Switzerland*, 9–11.
- 376 Newman, M. E., 2005: Power laws, pareto distributions and zipf’s law. *Contemporary Physics*, **46** (5), 323–351.
- 377 Oke, T. R., 1973: City size and the urban heat island. *Atmospheric Environment (1967)*, **7** (8), 769–779.
- 378 Oke, T. R., 1982: The energetic basis of the urban heat island. *Quarterly Journal of the Royal Meteorological Society*,  
379 **108** (455), 1–24.
- 380 Oleson, K., A. Monaghan, O. Wilhelmli, M. Barlage, N. Brunzell, J. Feddema, L. Hu, and D. Steinhoff, 2015: Interac-  
381 tions between urbanization, heat stress, and climate change. *Climatic Change*, **129** (3-4), 525–541.
- 382 Peel, M. C., B. L. Finlayson, and T. A. McMahon, 2007: Updated world map of the köppen-geiger climate classifica-  
383 tion. *Hydrology and Earth System Sciences*, **4** (2), 439–473.
- 384 Peng, S., and Coauthors, 2011: Surface urban heat island across 419 global big cities. *Environmental Science &*  
385 *Technology*, **46** (2), 696–703.
- 386 Robinson, P. J., 2001: On the definition of a heat wave. *Journal of Applied Meteorology*, **40** (4), 762–775.
- 387 Rosenzweig, C., W. Solecki, S. A. Hammer, and S. Mehrotra, 2010: Cities lead the way in climate-change action.  
388 *Nature*, **467** (7318), 909.
- 389 Rozenfeld, H. D., D. Rybski, J. S. Andrade, M. Batty, H. E. Stanley, and H. A. Makse, 2008: Laws of population  
390 growth. *Proceedings of the National Academy of Sciences*, pnas-0807435 105.
- 391 Sahimi, M., and M. Sahimi, 2014: *Applications of percolation theory*. CRC Press.
- 392 Schwarz, N., U. Schlink, U. Franck, and K. Großmann, 2012: Relationship of land surface and air temperatures and its  
393 implications for quantifying urban heat island indicatorsan application for the city of leipzig (germany). *Ecological*  
394 *Indicators*, **18**, 693–704.
- 395 Seto, K. C., and J. M. Shepherd, 2009: Global urban land-use trends and climate impacts. *Current Opinion in Envi-*  
396 *ronmental Sustainability*, **1** (1), 89–95.
- 397 Seto, K. C., and Coauthors, 2012: Urban land teleconnections and sustainability. *Proceedings of the National Academy*  
398 *of Sciences*, **109** (20), 7687–7692.
- 399 Shreevastava, A., P. S. C. Rao, and G. S. McGrath, 2018: Spatial analysis of the surface urban heat island. *Land*  
400 *Surface and Cryosphere Remote Sensing IV*, International Society for Optics and Photonics, Vol. 10777, 107770C.
- 401 Stewart, I. D., and T. R. Oke, 2012: Local climate zones for urban temperature studies. *Bulletin of the American*  
402 *Meteorological Society*, **93** (12), 1879–1900.
- 403 Voogt, J. A., and T. R. Oke, 2003: Thermal remote sensing of urban climates. *Remote Sensing of Environment*, **86** (3),  
404 370–384.
- 405 Walawender, J. P., M. J. Hajto, and P. Iwaniuk, 2012: A new arcgis toolset for automated mapping of land surface  
406 temperature with the use of landsat satellite data. *Geoscience and Remote Sensing Symposium (IGARSS), 2012 IEEE*  
407 *International*, IEEE, 4371–4374.

- 408 Weng, Q., 2003: Fractal analysis of satellite-detected urban heat island effect. *Photogrammetric Engineering & Re-*  
409 *mote Sensing*, **69** (5), 555–566.
- 410 Yang, S., K. Paik, G. S. McGrath, C. Urich, E. Krueger, P. Kumar, and P. S. C. Rao, 2017: Functional topology of  
411 evolving urban drainage networks. *Water Resources Research*, **53** (11), 8966–8979.
- 412 Zhou, B., D. Rybski, and J. P. Kropp, 2013: On the statistics of urban heat island intensity. *Geophysical Research*  
413 *Letters*, **40** (20), 5486–5491.
- 414 Zhou, B., D. Rybski, and J. P. Kropp, 2017: The role of city size and urban form in the surface urban heat island.  
415 *Scientific Reports*, **7** (1), 4791.
- 416 Zhou, W., G. Huang, and M. L. Cadenasso, 2011: Does spatial configuration matter? understanding the effects of land  
417 cover pattern on land surface temperature in urban landscapes. *Landscape and Urban Planning*, **102** (1), 54–63.

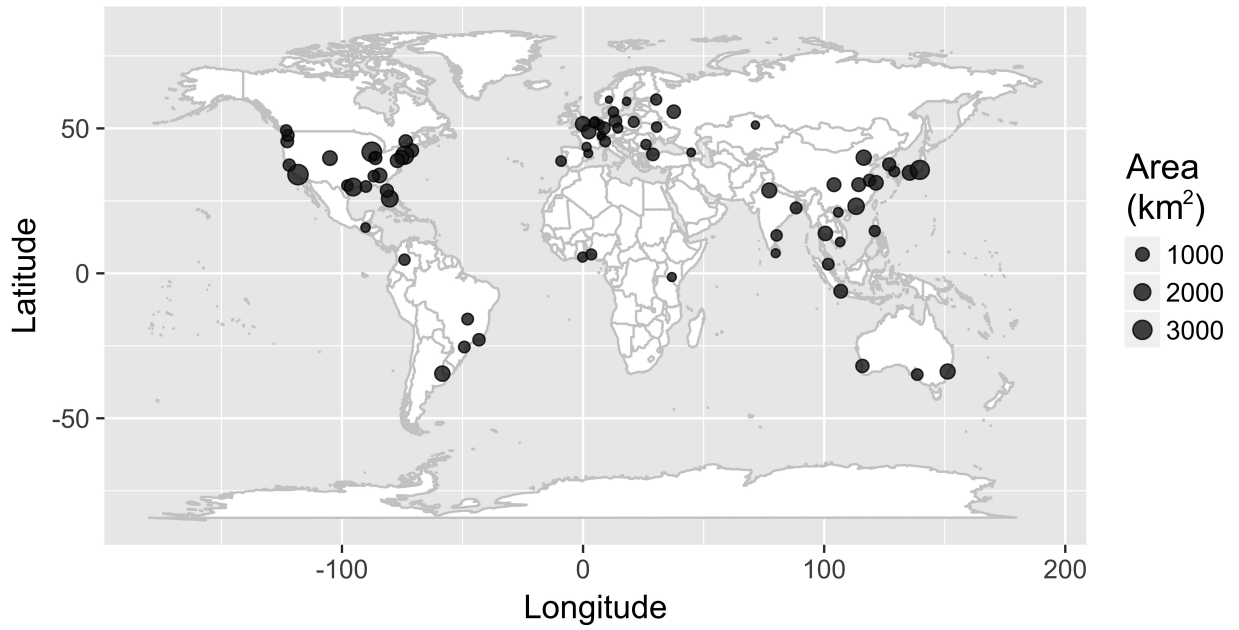
418 **Figures**

Figure 1: Map of the selected 78 cities chosen for this study. The size of marker is an indicator of the area of cities measured using the Urban land use class of MODIS Land Cover Type dataset.

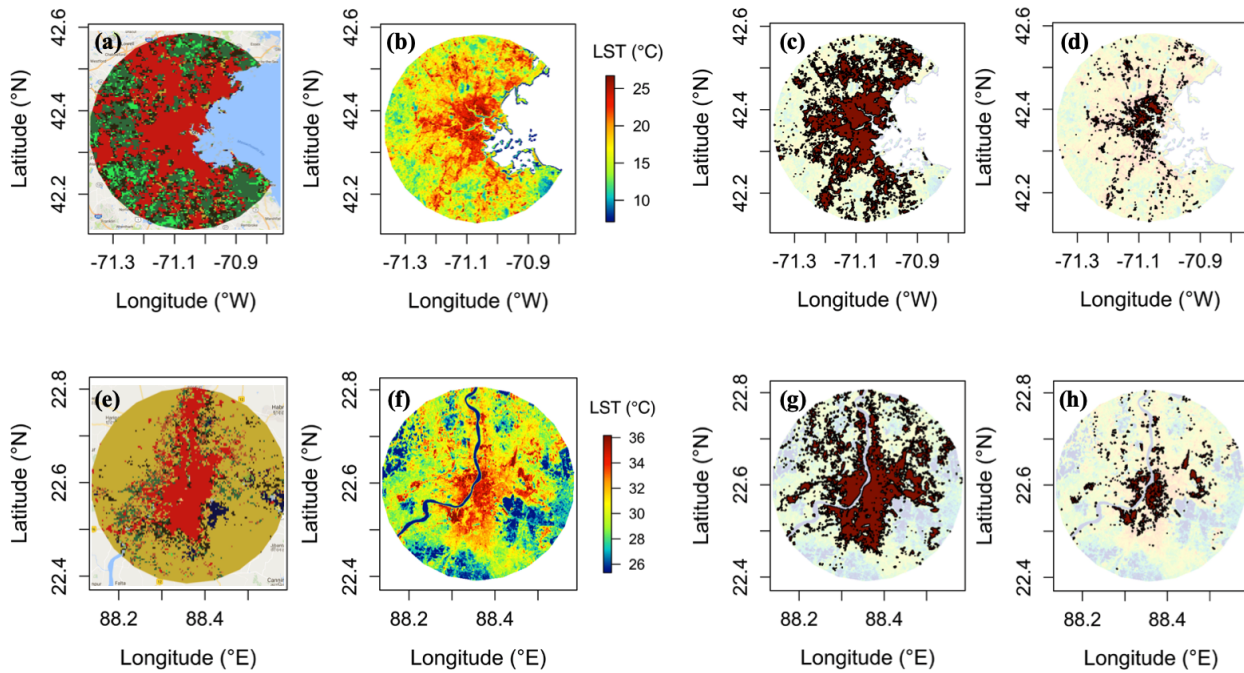


Figure 2: Maps for Boston (top) and Kolkata (bottom) are shown here as examples. (a, e) Land use map derived from MODIS - Land Cover Type dataset for the year 2016. (b, f) Land Surface Temperature (in °C) map derived from Landsat 8. (c, g) Clusters of high heat (Islets) above the statistical mode of temperatures, i.e. the most frequently encountered temperature (19°C for Boston and 32°C for Kolkata) obtained using Moore neighborhood clustering algorithm are indicated as red. (d,h) Extreme high heat islets obtained at the 95th percentile temperature of each city. Note the irregularity in the islets' perimeters and the disparity in their sizes.

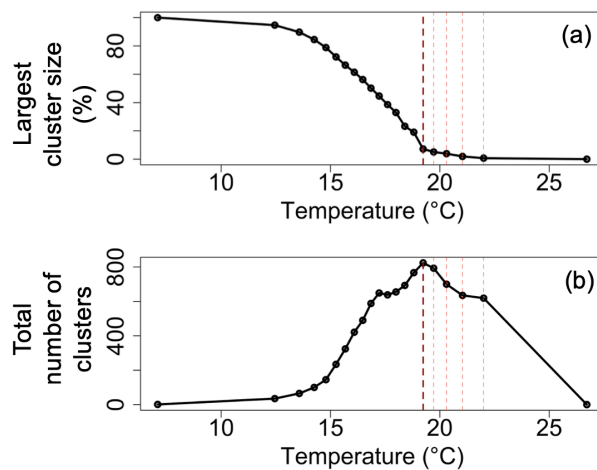


Figure 3: (a) Plot of largest cluster size as a function of thermal threshold for the case of Boston city (b) Total number of clusters shown for each thermal threshold. The first dashed red line shows the percolation threshold (75<sup>th</sup> percentile in this case) identified as the threshold where the total number of clusters is the maximum and below which the largest connected component emerges. Lighter red lines towards its right mark the subsequent percentiles of threshold which were considered for the analysis.

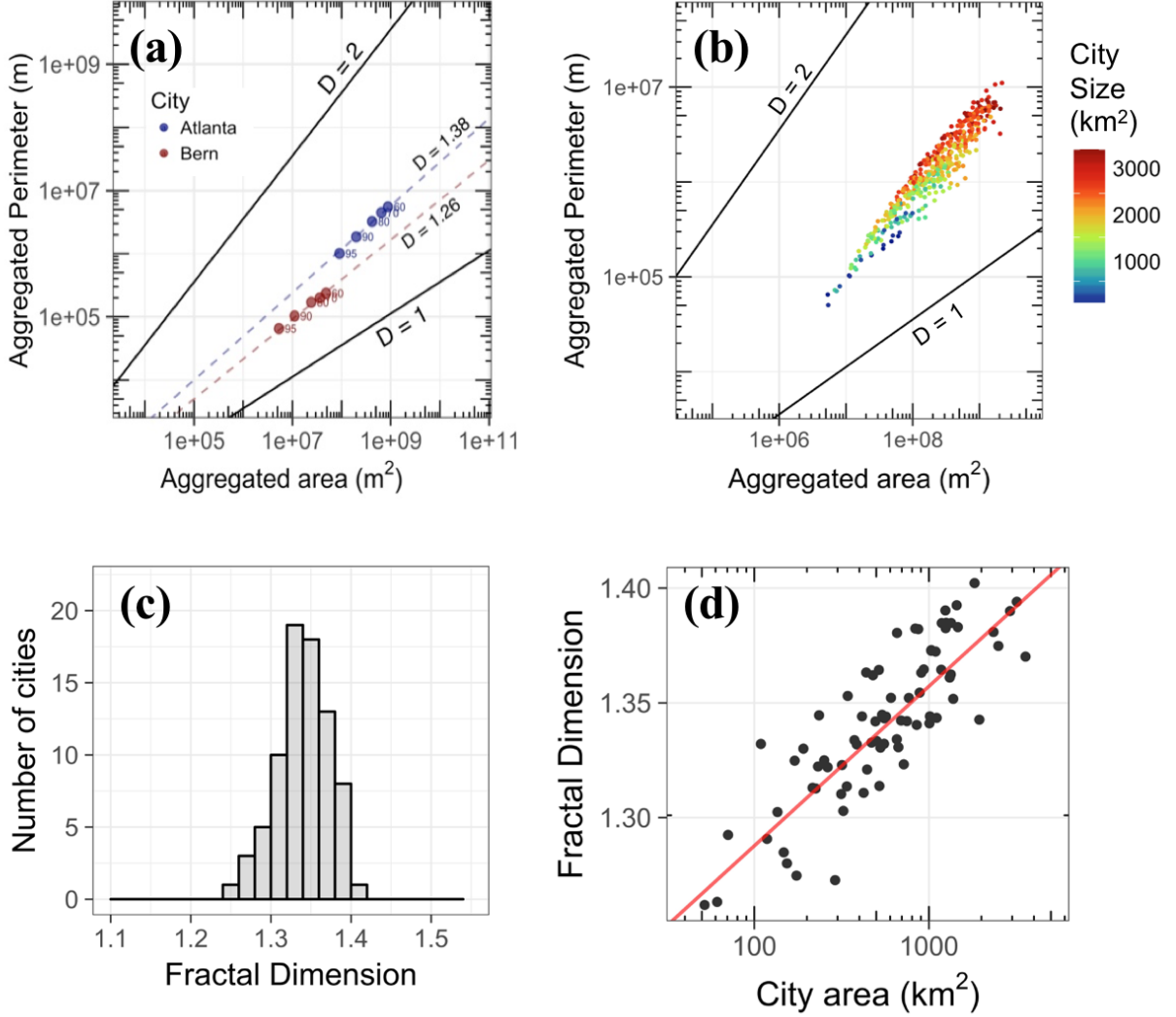


Figure 4: (a) Aggregated perimeters versus aggregated areas at 60, 70, 80, and 90 percentiles thresholds are shown here for two cities, Bern (in red) and Atlanta (in blue), demonstrating the same ratio of  $\log(\text{Area})$  and  $\log(\text{Perimeter})$  and hence the same Fractal Dimension ( $D$ ) of iso-thermal contour lines as indicated by the grey, dashed lines show examples of two cities with  $D = 1.38$  for Atlanta and  $D = 1.26$  for Bern.  $D$  of the perimeter of a circle ( $D = 1$ ) and a space-filling plane ( $D = 2$ ) are plotted to show the physical bounds for  $D$ . (b) The same plot for all cities shown with a single colour attributed to each city that corresponds to its area. (c) Histogram of  $D$  for all cities at their respective percolation thresholds with mean =  $1.33 \pm 0.007$  (95 % CI). (d)  $D$  as a function of the city area. This plot serves to illustrate that  $D$  increases with city area as per  $D = 0.0695 \log A_{\text{city}} + 1.15$  ( $R^2 = 0.7$ ).

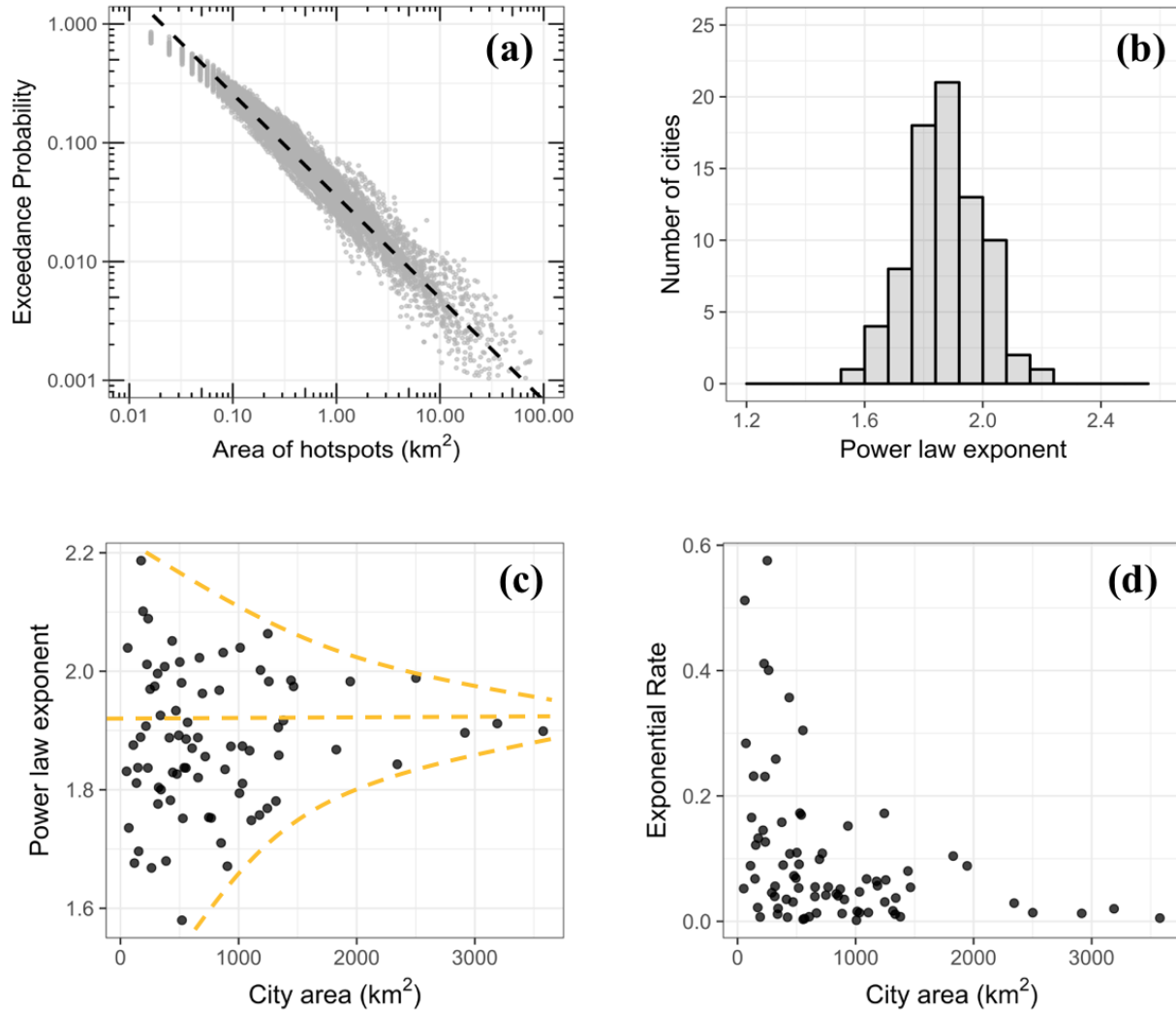


Figure 5: (a) Area Exceedance Probability Distributions for all cities at their respective percolation threshold are shown here in grey. Overlaid as a dashed black line is the line demonstrating the mean scaling exponent,  $\beta = 1.88$ . (b) A histogram of  $\beta$  of all cities. (c) Scatter plot of  $\beta$  and city area for each city. Yellow dashed lines serve to highlight this convergence of  $\beta$  to mean with an increase in the city area. (d) Scatter plot of mean exponential tempering coefficient,  $\bar{c}$ , calculated as an average of tempering coefficients ( $c$ ) obtained at temperatures above the percolation threshold. It is shown to rapidly decreasing to  $\bar{c} = 0$  with increasing city area. Each black dot represents a single city.



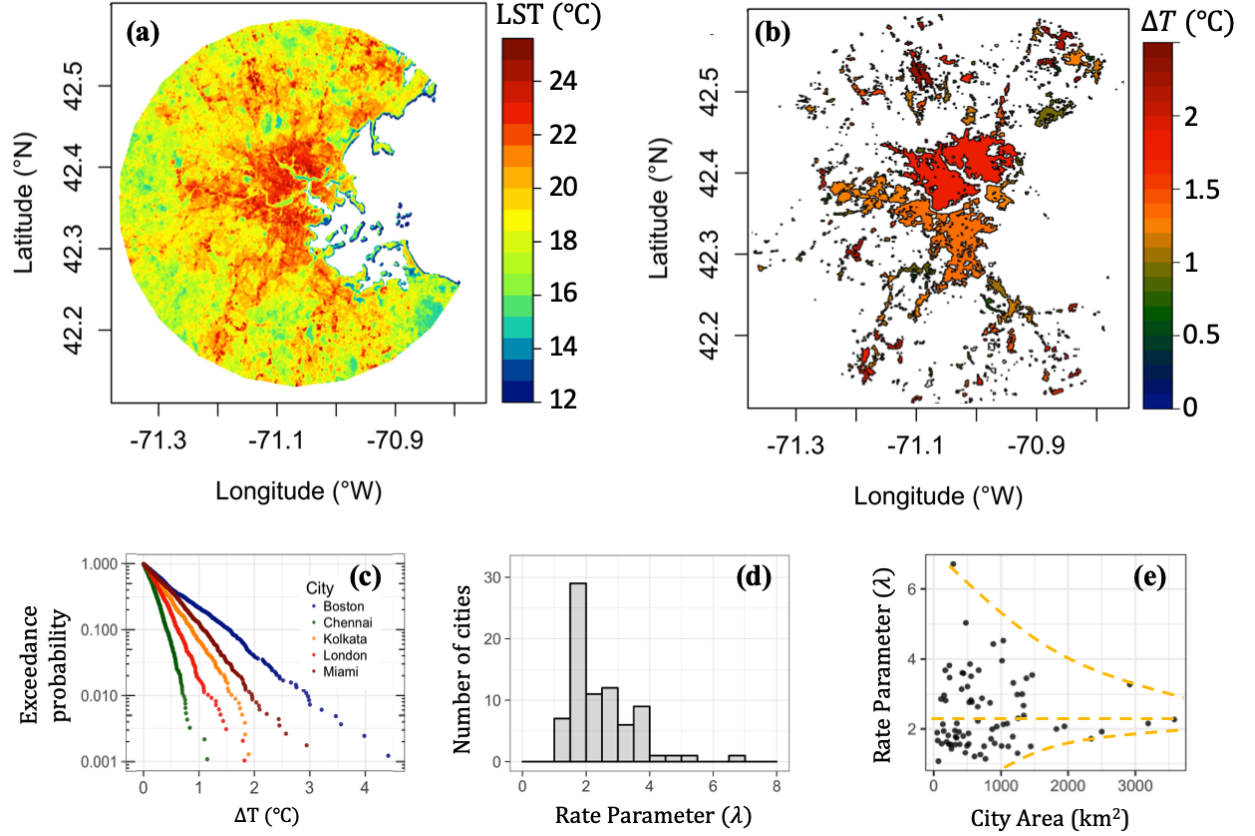


Figure 6: (a) Land Surface Temperature map of Boston (b) Map of heat islets obtained at mode temperature ( $19^{\circ}\text{C}$ , in this case) with colour representing the islet intensity ( $\Delta T$ ) above the mode. (c) Examples of empirical pdf of  $\Delta T$  for 5 selected cities shown on a semi-log graph at their respective mode temperatures to illustrate the disparity in exponential pdfs of  $\Delta T$ . Similar plot with all cities can be found as Figure S6. (d) Histogram of rate parameter  $\lambda$  (Eqn. 5) with mean =  $2.25\text{K}^{-1}$ . (e) Scatter plot of  $\lambda$  and area of all cities. Yellow dashed lines show the converging behaviour of  $\lambda$  with increasing area.

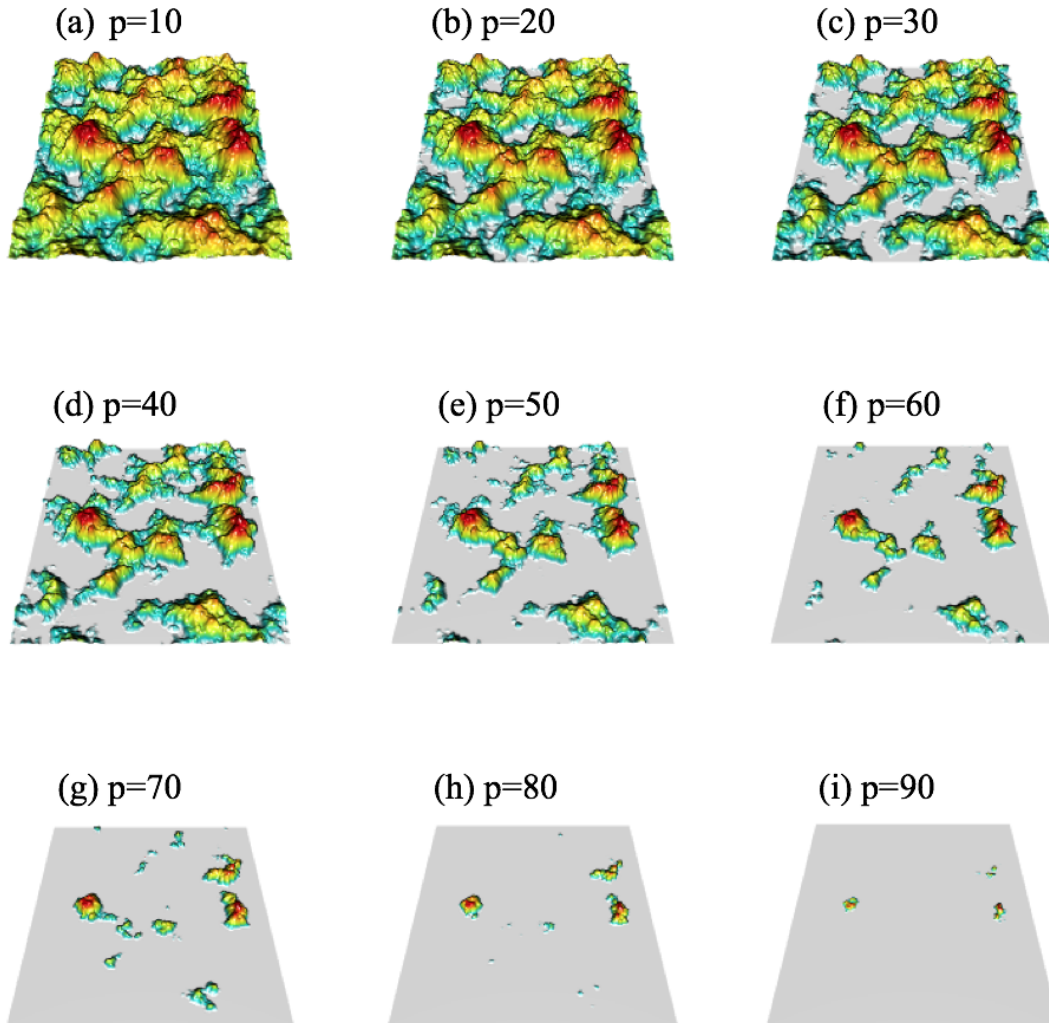


Figure 7: Illustrated above in an example of thresholding by percentile. The thermal maps are represented as 3-d elevation maps where height, as well as color, corresponds to a higher temperature. For each percentile of the thermal threshold, the areas above that are selected, and connected pixels (by Moore neighborhood) are grouped into a cluster. Figures (a-i) show the clusters that emerge above 9 incremental percentiles (shown as  $p$ , here).

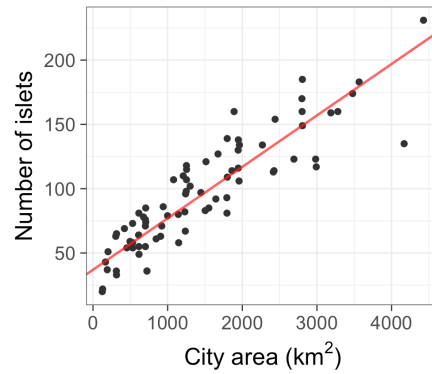


Figure 8: Scatter plot showing the correlation between number of islets and city size that scales linearly as  $N = 0.038 * A_{city} + 40$  ( $R^2 = 0.8$ ) as indicated by the red line.

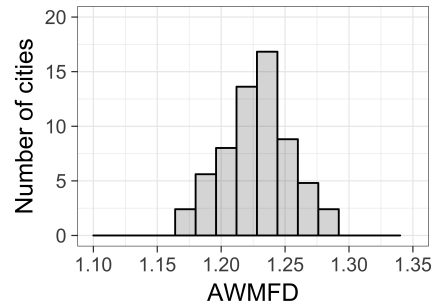


Figure 9: Histogram of Area Weighted Mean Fractal Dimension (AWMFD) for 78 cities.

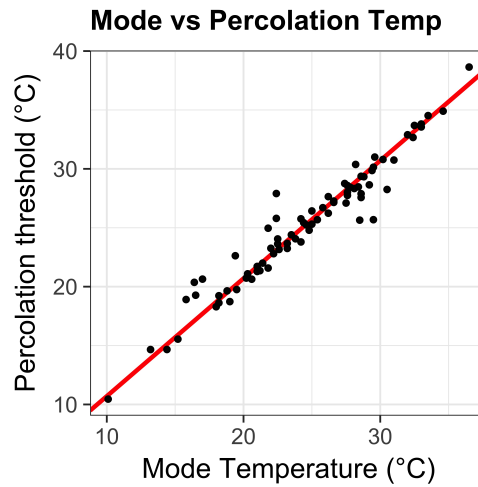


Figure 10: Scatter plot showing the correlation between mode temperature and the percolation threshold ( $R^2 = 0.93$ )